ACS APPLIED MATERIALS & INTERFACES

www.acsami.org Research Article

# Textured Lead-Free Piezoelectric Ceramics for Flexible Energy Harvesters

Yuvasree Purusothaman, Haoyang Leng, Aman Nanda, Ilan Levine, and Shashank Priya*

**Cite This:** *ACS Appl. Mater. Interfaces* 2023, 15, 6584−6593 Read Online

ACCESS | Metrics & More | Article Recommendations | SI Supporting Information

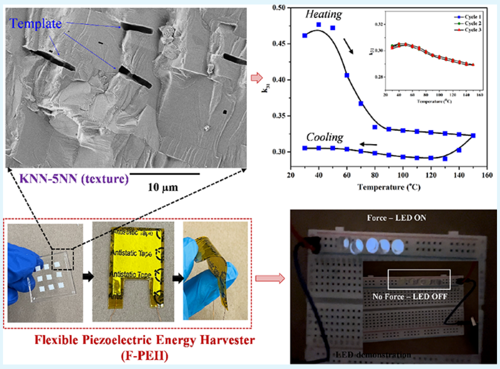

**ABSTRACT:** A lead-free (K,Na)$NbO_3$-based piezoelectric ceramic is textured along the (001) direction using the $NaNbO_3$ (NN) seeds. The composition $0.96(K_{0.5}Na_{0.5})(Nb_{0.965}Sb_{0.035})O_3-0.01CaZrO_3-0.03(Bi_{0.5}K_{0.5})HfO_3$ (KNN) is found to provide an excellent combination of electromechanical coefficients at room temperature. The textured composition with 5 wt % NN template (KNN-5NN) exhibits considerably improved electromechanical coefficients, $d_{33} \sim 590$ pC/N, $k_{31} \sim 0.46$, and $d_{31} \sim 215 \times 10^{-12}$ C/N, at room temperature. A flexible piezoelectric energy harvester (F-PEH) is fabricated using the textured KNN-5NN ceramic and tested under cyclic force. F-PEH exhibits enhanced output voltage ($V_{oc} \sim 25$ V), current ($I \sim 0.4$ $\mu$A), and power density ($P_D \sim 5.5$ mW/m$^2$) ($R_L$ of 10 MΩ) in the off-resonance frequency regime. In comparison to the random ceramic KNN-0NN-based F-PEH ($V_{oc} \sim 8$ V and $I \sim 0.1$ $\mu$A), the textured F-PEH significantly outperformed energy harvesting capability due to the large figure-of-merit value ($d_{31} \times g_{31}$) $\sim 3354 \times 10^{-15}$ m$^3$/J. This work provides a methodology for texturing lead-free materials and further implementing them in flexible energy harvesting devices and sensors.

**KEYWORDS:** *KNN piezoceramics, texture, phase transition, fatigue, flexible energy harvester*

Downloaded via PENNSYLVANIA STATE UNIV on January 21, 2024 at 16:57:15 (UTC).
See https://pubs.acs.org/sharingguidelines for options on how to legitimately share published articles.

## ■ INTRODUCTION

Energy harvesting (EH) approaches using piezoelectric, triboelectric, photovoltaic, and thermoelectric/pyroelectric effects have emerged as a promising solution for low-power consumer electronic devices.[1−5] Piezoelectric energy harvesters (PEHs) have gained importance for capturing naturally available vibrations, sound waves, human body movements, and various types of fluid flows.[6−8] The performance of the PEH primarily relies on the properties of the piezoelectric materials.[9] Among the various choices for piezoelectric materials, lead-rich perovskites near the morphotropic phase boundary (MPB) such as PZT, PZN-PT, PMN-PT, and PIN-PMN-PT have been pursued for enhancing the figure of merit.[10] Recently, in some countries, there are regulations under discussion on restricting the use of lead in the consumer devices.[11] Thus, it is imperative that any future developments of energy harvesting devices should consider the use of lead-free materials. Based on the environmental considerations, the focus in the area of lead-free materials has been primarily on four systems: (Bi,Na)$TiO_3$, $BaTiO_3$, $BiFeO_3$, and (K,Na)$NbO_3$.[12,13]

Perovskite-structured $K_xNa_{1-x}NbO_3$ (KNN) ceramics are considered as a promising lead-free material owing to their high Curie temperature ($T_c > 400$ °C) and excellent dielectric and piezoelectric properties.[14] However, challenges related to poor densification and volatilization of alkali metals at high temperatures limit the piezoelectric performance of $K_{0.5}Na_{0.5}NbO_3$ ceramics and, in most of the studies, the piezoelectric coefficient ($d_{33}$) has been reported to be ~110 pC/N.[14,15] Generally, $K_{0.5}Na_{0.5}NbO_3$ is modified through solid solutions and dopants to obtain a larger magnitude of product $d_{ij} \times g_{ij}$, which is necessary to achieve the higher figure of merit (FOM) in PEHs. Approaches such as chemical modifications with dopants, tuning of the phase boundaries, the addition of sintering aids, texture engineering, and processing techniques are widely adopted to enhance the dielectric and piezoelectric properties of KNN ceramics.[16,17]

Doping of $LiNbO_3$ or $LiTaO_3$ in the KNN composition has been shown to provide an improved $d_{33}$ of up to 200−280 pC/N while maintaining a high $T_c \sim 452−510$ °C.[18] By compositionally designing new rhombohedral (R)−orthorhombic (O)−tetragonal (T) phase boundaries, the $d_{33}$ has been shown to increase to 344−425 pC/N with reduced $T_c <$ 200 °C.[14,16,19] Using the reactive grain growth method (RGG), a large $d_{33}$ of ~416 pC/N has been achieved in $Li^+$-, $Ta^{5+}$-, and

**Received:** August 30, 2022
**Accepted:** January 10, 2023
**Published:** January 24, 2023

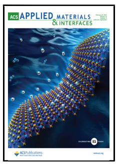

ACS Publications © 2023 American Chemical Society

https://doi.org/10.1021/acsami.2c15640
ACS Appl. Mater. Interfaces 2023, 15, 6584−6593

$Sb^{5+}$-modified KNN ceramics having $T_c$ of ≤220 °C.[20] Recently, the KNN composition has been shown to achieve an ultrahigh $d_{33}$ of ~700 pC/N and $T_c$ of ~242 °C through the template grain growth (TGG) technique using (001) $NaNbO_3$ platelets.[21] All the existing KNN-based studies indicate the crucial balance of having high thermal stability ($T_c$) along with large electromechanical constants ($k_{ij}$, $d_{ij}$, and $g_{ij}$), i.e., improving $d_{33}$ lowers temperature stability and vice versa. Due to the presence of polymorphic phase transition (PPT) in the KNN system, there is a narrow window for optimization of the thermal stability and electromechanical constants in KNN compositions.[14] Textured KNN piezoceramics, like any other ceramics, have brittle nature, which further imposes challenges in their implementation for PEH.[22] Thus, in addition to material innovation, a new architectural design is also needed to ensure their reliability in PEH.

In this study, a flexible piezoelectric energy harvester (F-PEH) is demonstrated using a high-performance textured lead-free KNN piezoceramic. The formulation $0.96(K_{0.5}Na_{0.5})(Nb_{0.965}Sb_{0.035})O_3{-}0.01CaZrO_3{-}0.03(Bi_{0.5}K_{0.5})HfO_3$ is textured using plate-like $NaNbO_3$ (NN) templates. Dielectric and piezoelectric properties of the KNN-$x$NN ($x$ = 0, 3, 5, and 7 wt %) materials are investigated as a function of sintering temperature and texturing degree. The textured KNN-5NN ceramic is found to exhibit high $d_{33}$ of ~590 pC/N with $T_c$ above 240 °C, enhanced electromechanical coupling factor ($k_{31}$) ~ 0.46, and piezoelectric charge constant ($d_{31}$) ~ $215 \times 10^{-12}$ C/N. In comparison, the random KNN-0NN ceramic exhibited $d_{33}$ ~ 270 pC/N. To understand the thermal stability of this composition, electromechanical measurements are conducted over the temperature range of 25 to 150 °C. The F-PEH is fabricated using an 18 wt % KNN-$x$NN ceramic in a PDMS polymeric matrix to harness environmentally available biomechanical energy. The F-PEH developed using textured KNN-5NN generates higher voltage, $V_{oc}$ ~ 25 V, and current, $I$ ~ 0.4 $\mu$A, compared to the random KNN-0NN-based F-PEH ($V_{oc}$ ~ 8 V and $I$ ~ 0.1 $\mu$A at 10 MΩ). The results demonstrate that the textured KNN-based piezoceramics can be employed as a potential candidate for developing high-power flexible energy harvesters and sensors near room temperature.

## EXPERIMENTAL PROCEDURE

**Synthesis of Random KNN (KNN-0NN).** The matrix powder with the formulation of $0.96(K_{0.5}Na_{0.5})(Nb_{0.965}Sb_{0.035})O_3{-}0.01CaZrO_3{-}0.03(Bi_{0.5}K_{0.5})HfO_3$ (designated as KNN here) was synthesized using a conventional solid-state reaction approach. Precursor reagents including $Na_2CO_3$ (Alfa Aesar, 99.5%), $K_2CO_3$ (Sigma-Aldrich, 99%), $Nb_2O_5$ (Sigma-Aldrich, 99.9%), $Sb_2O_3$ (Alfa Aesar, 99.6%), $Bi_2O_3$ (Alfa Aesar, 99%), $ZrO_2$ (Alfa Aesar, 99.7%), $CaCO_3$ (Sigma-Aldrich, 99%), and $HfO_2$ (Alfa Aesar, 99%) were accurately weighed in the stoichiometric ratio. All the raw materials were ball-milled with an appropriate amount of zirconia balls and ethanol for 24 h. The dried mixture was calcined at 850 °C for 6 h and then ball-milled again for 24 h in an ethanol medium. After drying at 100 °C for 4 h, the matrix powders were pressed into pellets and subjected to cold isostatic pressing at 200 MPa (CIP). Later, the pellets were sintered by a two-step sintering approach: heating up to 1190 °C (ramp rate of 5 °C/min), then cooling to 1090 °C (ramp rate of 10 °C/min), and holding for a 10 h dwell time. The optimized sintering conditions were determined in the temperature range between 1090 and 1130 °C with ±10 °C variations.

**Synthesis of Textured KNN (KNN-$x$NN, $x$ = 3, 5, and 7 wt %).** The texturing of KNN occurs through the template grain growth (TGG) method. A platelet like $NaNbO_3$ (NN) is used as a template, which is synthesized using the topochemical crystal conversion method (as reported in detail elsewhere).[23] To develop textured KNN, the calcined matrix powder was ball-milled for 24 h with polyvinyl butyral (PVB) as a binder and ethanol as a solvent. Next, the slurry was mixed with an appropriate amount of NN template (3, 5, and 7 wt %) and magnetically stirred for 2 h. The seeded slurry was tape-cast using a 230 $\mu$m doctor blade. The dried tape was cut, stacked, and laminated at 85 °C with 20 MPa pressure for 20 min. Later, the green compacts were heated at 400 °C (ramp rate of 0.5 °C/min) for 1 h to burn out the PVB binder. After the CIP, the samples were treated using a two-step sintering condition (as referred to the KNN-0NN synthesis section). Finally, the sintered samples (random and texture) were polished, diced to standard shapes, and coated with silver electrodes (using silver paste heated to 550 °C for 30 min). Before the electrical measurements, all the samples were electrically poled at room temperature under a DC field of 3 kV/mm for 10 min and aged for 24 h before measurements.

**Fabrication of the Flexible Piezoelectric Energy Harvester (F-PEH).** A planar F-PEH module was designed to investigate the performance of random and textured KNN-$x$NN ceramics. The active composite layer in the F-PEH was processed through the solution casting approach. A transparent homogeneous mixer of polydimethylsiloxane (PDMS) was prepared using the hardener in the ratio of 10:1. The textured KNN-5NN sample in the amount of 18 wt % was used as a filler material. Each KNN-5NN ceramic was diced to 3 mm ($l$) × 3 mm ($w$) × 0.5 mm ($t$) plates and then dispersed in the PDMS matrix. The final solution of KNN-5NN/PDMS was poured into a smooth glass dish (with the prescribed arrangement of the diced ceramics) and dried in the hot-air oven at 75 °C for 1 h. The solidified film was peeled off and cut into the required dimension of the F-PEH device (2 cm × 2 cm). The processed flexible KNN-5NN/PDMS film was sandwiched between the thin aluminum (Al) foil electrodes using the hot-press technique for 1 h. For electrical measurements, two copper (Cu) wires were attached to the top and bottom Al electrodes using silver paste. Later, the F-PEH was packed using a Kapton film to protect the device from extrinsic physical damage. Prior to the Kapton encapsulation, the antistatic film was attached to both the Al electrodes to circumvent the electrostatic potential generation between Al−Kapton interfaces. Last, the device was electrically poled at 6 kV for 12 h at room temperature. Similarly, 18 wt % KNN-0NN-based F-PEH was fabricated and poled to compare the performance of random and textured piezoceramics-based devices.

**Characterizations.** The crystal phase structure and orientation degree were determined through a PANalytical Empyrean X-ray powder diffraction system at 40 kV/40 mA using Cu K$\alpha$ radiation at 1.5406 Å (XRD, Philips, Almelo, Netherlands). The in situ temperature-dependent X-ray diffraction patterns were collected using a Co K$\alpha_{1-2}$ (1.789010/1.792900 Å) diffractometer equipped with an Anton Paar HTK 1200N non-ambient chamber. The microstructural analysis was carried out using field emission scanning electron microscopy equipped with electron backscatter diffraction (FESEM/EBSD, FEI Quanta 600 FEG, FEI). The piezoelectric coefficient ($d_{33}$) was measured using a quasi-static piezometer, YE 2730 A (APC Products, Inc., PA). The temperature-dependent dielectric permittivity ($\varepsilon_r$) and dissipation factor (tan $\delta$) were tested by an LCR meter at 1 kHz (HP4274A, Hewlett-Packard, Palo Alto, CA). The electromechanical coupling factor ($k_{31}$) and piezoelectric constants ($d_{31}$) were determined using the resonance ($f_r/f_m$) and anti-resonance frequencies ($f_a/f_n$) obtained through an impedance analyzer (HP4194A, Hewlett-Packard, Palo Alto, CA). The polarization hysteresis loops (P−E) and strain curves (S−E) of the KNN-$x$NN ceramics were tested by a ferroelectric test system (Precision Premier II, Radiant Technology, Inc., Albuquerque, NM) enabled by a high-voltage power supply (Trek 609B, Lockport, NY). The output electrical signals from the fabricated F-PEH devices were measured using a digital oscilloscope (DSOX4024A, Keysight) by applying constant mechanical force.

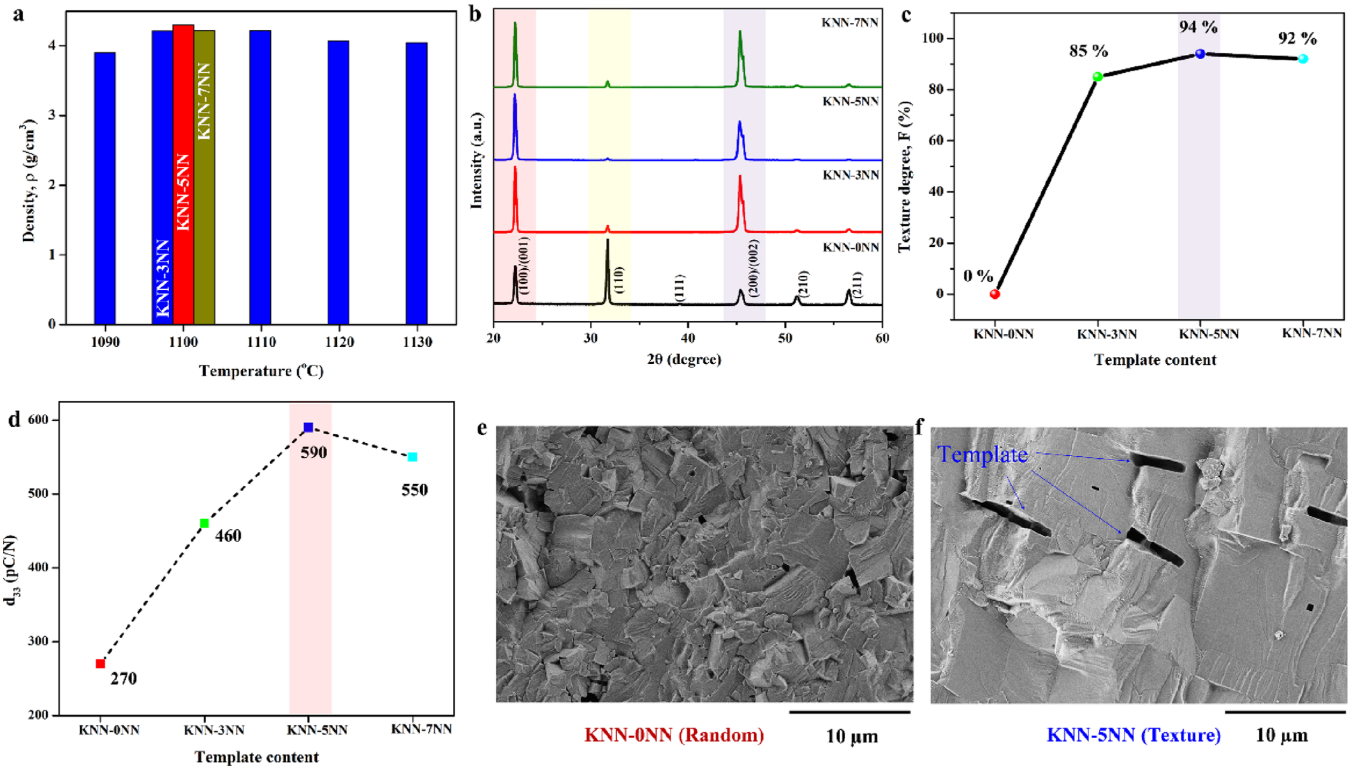

**Figure 1.** (a) Density of KNN-$x$NN as a function of sintering temperature and NN template ratio. (b) XRD patterns of KNN-$x$NN ($x$ = 0, 3, 5, and 7 wt %) piezoceramics. (c) Texture degree relative to NN template concentration. (d) $d_{33}$ values as a function NN wt %. (e) FESEM image of KNN-0NN showing random grain alignment. (f) FESEM image of KNN-5NN showing (001) NN template-oriented grain growth.

## ■ RESULTS AND DISCUSSION

Figure S1 schematically illustrates the synthesis procedures of KNN-$x$NN ceramics ($x$ = 0, 3, 5, and 7 wt % NN template). Figure S2a shows the XRD pattern of the NN template synthesized through the topochemical conversion method, indicating a perovskite phase with strong orientation along the (001) and (110) planes.[23] The microstructural image in Figure S2b reveals the plate-like NN particles with an average length of ~15 μm and a thickness of ~1 μm. Figure 1a compares the density of textured KNN samples as a function of sintering condition (1090−1130 °C) and NN wt %. To evaluate the sintering effect, KNN-3NN compositions are used, for which densification and grain growths are found to be optimum at 1100 °C. As the sintering temperature increases (>1100 °C), the density declines due to the formation of pores as an effect of volatilization.[24] The density ($\rho$) considerably improves as the template content is increased to 5 wt % (KNN-5NN ~ 4.297 g/cm$^3$) with a relative density of 94.5% as shown in Figure S3a.

Figure 1b shows the room-temperature XRD patterns of KNN-$x$NN samples sintered at 1100 °C with various NN wt %. As seen in the figure, all samples exhibit a perovskite phase with no secondary phases. The peak splitting at 45° indicates that the samples have mixed O−T phases with predominant orthorhombic symmetry as the calculated $I_{002}/I_{200}$ intensity ratios are ≤1.75.[21] In comparison to the random samples, the textured KNN samples show a higher intensity peak corresponding to (001) planes. This indicates the crystallographic orientation along the (001) axial plane. The corresponding texture degree is calculated from the Lotgering factor (LF) given as[25,26]

$$F_{(00l)} = \frac{P_{(00l)} - P_0}{1 - P_0} \tag{1}$$

$$P_{(00l)} = \frac{\sum I_{(00l)}}{\sum I_{(hkl)}} \tag{2}$$

$$P_0 = \frac{\sum I_{0(00l)}}{\sum I_{0(hkl)}} \tag{3}$$

where $\sum I_{(00l)}$ and $\sum I_{(hkl)}$ are the summation of XRD peak intensities of (001) and ($hkl$) planes of the textured KNN piezoceramic, and $\sum I_{0(00l)}$ and $\sum I_{0(hkl)}$ represent the summation of intensities for peaks (001) and ($hkl$) of randomly oriented KNN piezoceramics, respectively. The LF calculation shows that the maximum texture degree, $F$ ~ 94%, is obtained for KNN-5NN compared to $F$ ~ 85% for KNN-3NN and $F$ ~ 92% for KNN-7NN (Figure 1c). The template volume affected the percentage of mixed phase symmetry, which is evident from the $I_{002}/I_{200}$ intensity ratios of 1.75, 1.5, and 1.6 for KNN-3NN, KNN-5NN, and KNN-7NN, respectively.[26,27] With a high LF factor, KNN-5NN exhibits a 2-fold increase in $d_{33}$ ~ 590 pC/N compared to that of random ~270 pC/N (Figure 1d). Figure 1e,f displays the FESEM images of thermally etched surfaces of the random KNN-0NN and textured KNN-5NN samples. The microstructures of KNN-3NN and KNN-7NN samples are supplemented in Figure S4. The aligned NN platelets in the KNN matrix (by the doctor blade tape casting process) promote the grain development along the (001) direction.[24] The TGG process facilitates the KNN epitaxial grain growth around the NN template interfaces. This results in the formation of a highly oriented polycrystalline structure

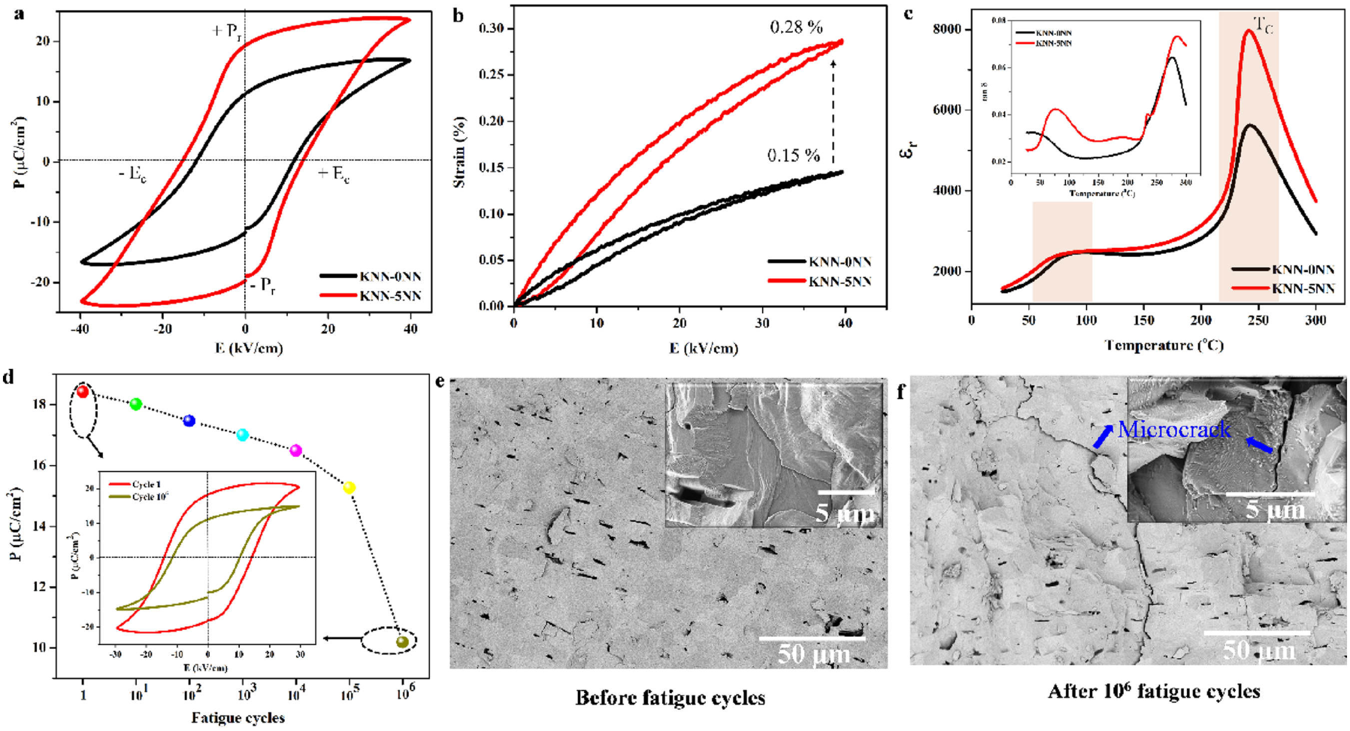

Before fatigue cycles

After 10⁶ fatigue cycles

**Figure 2.** (a) Ferroelectric hysteresis (P−E) loops of KNN-*x*NN ($x = 0$ and 5 wt %) ceramics. (b) Unipolar strain−electric field (S−E) loops of KNN-0NN and KNN-5NN samples. (c) Temperature-dependent dielectric loops of random and 5 wt % textured ceramics measured at 25−300 °C. Inset: dielectric loss (tan $\delta$) curves. (d) Electric fatigue behavior of KNN-5NN at 30 kV/cm. Inset: P−E loop for 1 and $10^6$ cycles. FESEM images of the KNN-5NN ceramic (e) before and (f) after fatigue analysis.

with brick-like larger grains compared to the nontextured ceramic.[28] Further, Figure S5 confirms the strong (001) orientation of grains in the textured KNN-5NN ceramic through the EBSD mapping analysis.

Figure 2a displays the room-temperature polarization−electric field hysteresis loops (P−E) for the KNN-*x*NN ceramics ($x = 0$ and 5 wt %) measured at 40 kV/cm electric field (1 Hz). It should be noted that textured materials have phase transition closer to room temperature as compared to random ceramics; thus, the measurement captures the influence of shift in transition state on the loss behavior. The remnant polarization tends to increase in the textured ceramics as a function of increased NN template content (Figure S3b). This can be ascribed to the fact that the crystallographic grain orientation promoted through texturing enables improved piezoelectric properties.[29] Specifically, the KNN-5NN ceramic maintains a high degree of remnant order with the $P_r$ and $E_c$ values of ~19.34 $\mu$C/cm$^2$ and ~13.72 kV/cm, respectively. The $P_r$ gradually decreases with a further increase in the template content to 7 wt %, indicating the weakening of piezoelectricity due to the composition change contributed by the antiferroelectric NN seeds.[24] The P−E loops with the field-dependent stability of KNN-5NN are presented in Figure S6a in the range of 30−70 kV/cm.

The unipolar strain−electric field (S−E) loops of the random and texture ceramics are shown in Figure 2b. The maximum strains achieved at 40 kV/cm are 0.28 and 0.15% for KNN-5NN and KNN-0NN samples, respectively. The corresponding high-field piezoelectric strain coefficient ($d_{33}$*) is calculated as the maximum strain/maximum field ($S_{max}$/$E_{max}$) and is found to be 725 and 375 pm/V for KNN-5NN and KNN-0NN ceramics, respectively. Figure 2c shows the temperature-dependent dielectric permittivity ($\varepsilon_r$−$T$) of random and textured ceramics in the temperature range of 25−300 °C; herein, the 1 kHz data is shown. For both KNN-0NN and KNN-5NN samples, two dielectric peaks are observed around ~70 and ~240 °C corresponding to two phase transitions, i.e., orthorhombic to tetragonal ($T_{O-T}$) and tetragonal to cubic ($T_c$). The slight shift in both peaks can be related to the lattice distortion due to the texturing effects using 5 wt % NN templates.[25] In addition, it can be observed that KNN-5NN exhibits an improved dielectric permittivity ($\varepsilon_{max} \sim 7965$) and low room-temperature dielectric loss (tan $\delta$ < 2.5%) in comparison to KNN-0NN (tan $\delta$ ~ 3.2%). The intrinsic piezoelectric properties of the ceramic can be expressed according to the equation

$$d_{33} = 2Q\varepsilon_0\varepsilon_{33}P \tag{4}$$

where $Q$ is the electrostrictive constant, $\varepsilon_0$ is the vacuum permittivity, $\varepsilon_{33}$ is the permittivity of the material, $P$ is the remanent polarization, and $d_{33}$ is the piezoelectric coefficient.[30] Based on eq 4, the improved dielectric and polarization parameters exhibited by the textured KNN-5NN sample result in its enhanced piezoelectric performance compared to the random counterpart. Table S1 summarizes the detailed properties of KNN-0NN and KNN-5NN ceramics.

As seen in Figure 2d, the electrical fatigue characteristics reveal a significant degradation of polarization after several cycles measured at room temperature. After exposing the material to $10^6$ cycles at 30 kV and 10 Hz, the remnant polarization decays by ~44% (from ~18.42 to 10.19 $\mu$C/cm$^2$). The P−E loops at the first cycle and $10^6$ cycles are compared in the inset of Figure 2d. The textured KNN-5NN shows a better fatigue behavior compared to the random KNN-0NN ceramic with a polarization decay rate of ~56% (Figure S7). The microstructures of samples before and after fatigue cycles

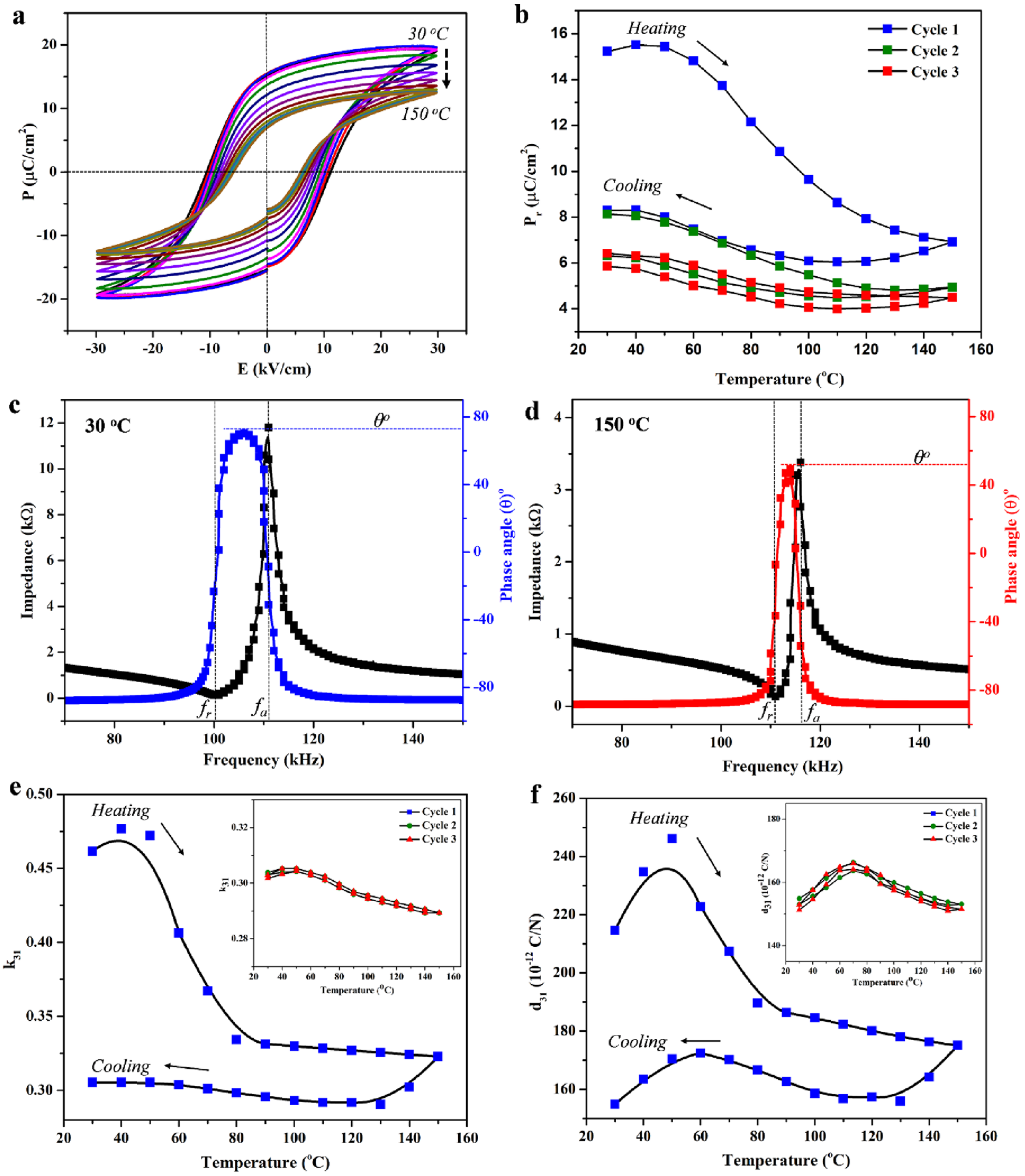

**Figure 3.** Temperature-dependent fatigue characteristics of the textured KNN-5NN ceramic over the range of 30−150 °C. (a) Temperature-based fatigue P−E loops at 30 kV/cm. (b) Comparative $P_r$ plot from the three fatigue cycles 1, 2, and 3. Frequency dependence of impedance $|Z|$ and phase angle $\theta°$ measured at (c) 30 °C and (d) 150 °C. (e) Electromechanical coupling factor ($k_{31}$) and (f) piezoelectric constant ($d_{31}$) of three heating−cooling cycles 1, 2, and 3.

are shown in Figure 2e,f. After the $10^6$ cycles, the microcracks are observed, which indicates that mechanical deterioration is the cause for the drop in polarization. Such degradation behavior is illustrated through fatigue models based upon domain wall pinning, dead layer deposition, and crack formations (Figure S8).[31]

To evaluate the operating temperature range of the KNN material, the thermal stability of KNN-5NN composition in the temperature range of 30 to 150 °C is investigated as shown in Figure 3. The P−E loops at different temperatures are measured with increasing temperature (heating cycle 1) as shown in Figure 3a, and its relative cooling cycle is shown in Figure S6c. The corresponding $P_r$ values at varying temperatures with 10 °C increments are plotted in Figure 3b. Initially, the $P_r$ remains high with a slight improvement as the temperature rises and then starts to decline as the temperature increases beyond 50 °C. The monotonous reductions in $P_r$ and $E_c$ suggest the significant fading of the piezoelectric properties in the KNN-5NN ceramic as it crosses over the $T_{O\text{-}T}$ phase boundary region. KNN-5NN shows degradation much before the actual transition occurring at ~70 °C.[17] Successive thermal analysis is repeated (cycles 2 and 3) with the sequence of heating and then cooling back to room temperature. The repeated heating and cooling cycle analysis exhibits the

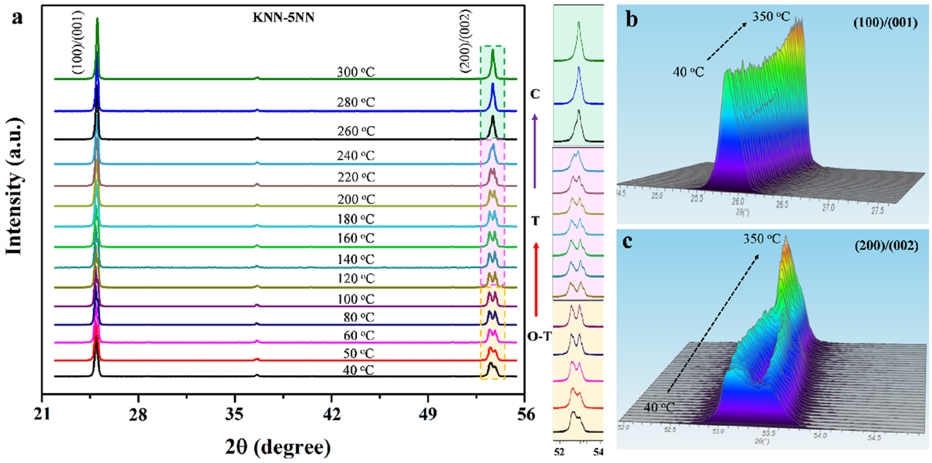

**Figure 4.** In situ temperature-dependent XRD analysis of the textured KNN-5NN ceramic. (a) Diffraction patterns at different temperatures ranging from 40 to 300 °C. Magnified 3D spectra of (b) (100)/(001) peaks and (c) (200)/(002) peaks illustrating the phase transitions for 10 °C intervals.

irreversible properties in KNN-5NN as a function of temperature. Figure 3c,d represents the temperature dependence of impedance (|Z|) and polarization phase angle ($\theta°$) measured at 30 and 150 °C for the KNN-5NN piezoceramic. The resonance ($f_r$) and anti-resonance ($f_a$) values show a reasonable bandwidth with a phase angle of ~73° at 30 °C. At a high temperature of 150 °C, the impedance spectrum narrows significantly, and the phase angle is reduced to ~51°. Using the resonance technique and dielectric parameters, the electromechanical coupling factor ($k_{31}$) and piezoelectric charge constant ($d_{31}$) are calculated using the following equations[32]

$$k_{31} = \sqrt{\frac{A}{1+A}}, \text{ where } A = \frac{\pi}{2}\cdot\frac{f_n}{f_m}\cdot\tan\left[\frac{\pi}{2}\cdot\frac{(f_n - f_m)}{f_m}\right] \tag{5}$$

$$d_{31} = k_{31}\sqrt{8.85\times 10^{-12}\cdot K_3^T\cdot s_{11}^E}, \text{ where } s_{11}^E = \frac{1}{4\cdot\rho\cdot f_m^2\cdot l^2} \tag{6}$$

where $f_n$ and $f_m$ are the frequencies of minimum impedance/resonance and maximum impedance/anti-resonance frequency, $K_3^T$ is the free relative dielectric constant, $s_{11}^E$ is the elastic compliance, $\rho$ is the density of the ceramic, and $l$ is the length of the sample. The $k_{31}$ (Figure 3e) and $d_{31}$ (Figure 3f) plots show similar temperature-dependent nature as observed for polarization variation. The KNN-5NN sample exhibits high $k_{31} \sim 0.46$ and $d_{31} \sim 215 \times 10^{-12}$ C/N at room temperature, which decrease gradually as a function of temperature. The initial room-temperature properties are not recovered after the thermal heating and cooling in cycle 1. The respective inset graph shows the stabilized performance after cycles 2 and 3 with loss of nearly 50% of polarization in the KNN-5NN ceramic. To understand this degradation mechanism, temperature-dependent XRD is performed to reveal the details of the phase transition process. Figure 4a presents the in situ temperature-dependent XRD spectra of the KNN-5NN ceramic in the temperature range of 40 to 350 °C. Figure 4b,c shows the enlarged 3D graph of the (100)/(001) and (200)/(002) peaks at every 10 °C interval. As shown here, the O−T phase coexists in the KNN-5NN ceramic in the temperature range of 40−100 °C. In this range, the (200) peak intensity keeps increasing, implying the transition of the O-to-T phase. With a further increase in the temperature range to 240 °C, the T phase becomes dominant as evident from the intensity value of $I_{(002)}/I_{(200)} \sim 0.78$ (Figure S9) given by[26,27]

$$\alpha_{\text{ortho}} = [(I_{011}/I_{100}) + (I_{022}/I_{200})]/2 \text{ (O symmetry} \sim 1.85) \tag{7}$$

$$\alpha_{\text{tetra}} = [(I_{001}/I_{010}) + (I_{002}/I_{020})]/2 \text{ (T symmetry} \sim 0.53) \tag{8}$$

Above 240 °C, the pseudocubic phase is observed by converging into a single peak. This illustrates the anomaly of the intensity peaks and the dielectric permittivity. Due to the phase transition behavior, depolarization occurs as the temperature exceeds the $T_{O-T}$ range and the tetragonal phase becomes more pronounced with a further increase in temperature.[33−35] A partial depoling is observed on the order of ~27% decrease in the piezoelectric constants during the first heating cycle (Figure 3), which is attributed to the changes in the domain configuration due to changes in crystallographic symmetry.[36−38] After cooling to room temperature, no significant increase or restoration in $k_{31}$ and $d_{31}$ is noticed due to restricted domain switching. Hence, to reorient the switched domains, electric repoling is performed, which restores the high degree of domain alignment, thereby resulting in the restoration of the enhanced piezoelectric properties (Figure S10).[39−41] The temperature-dependent unipolar S−E loops of random and textured ceramics are shown in Figure S11 at 40 kV/cm. It is noted that the strain variation of KNN-5NN (~20%) is less compared to that of KNN-0NN (~30%) over the temperature range of 30−150 °C. These results demonstrate the phase transition-dependent fatigue mechanisms affecting the operating range of KNN ceramics. Based on these results, it is clear that KNN materials synthesized in this study have a relevant performance below 50 °C. Applications such as energy harvesters and sensors are mostly operated below this temperature, and thus, the KNN-5NN ceramic provides an advantage in those scenarios.

A flexible piezoelectric energy harvester (F-PEH) is designed to harvest ambient biomechanical energy using the developed KNN material. The device is fabricated by integrating KNN-$x$NN as an active material embedded in the PDMS polymer matrix. The detailed fabrication procedure is discussed in

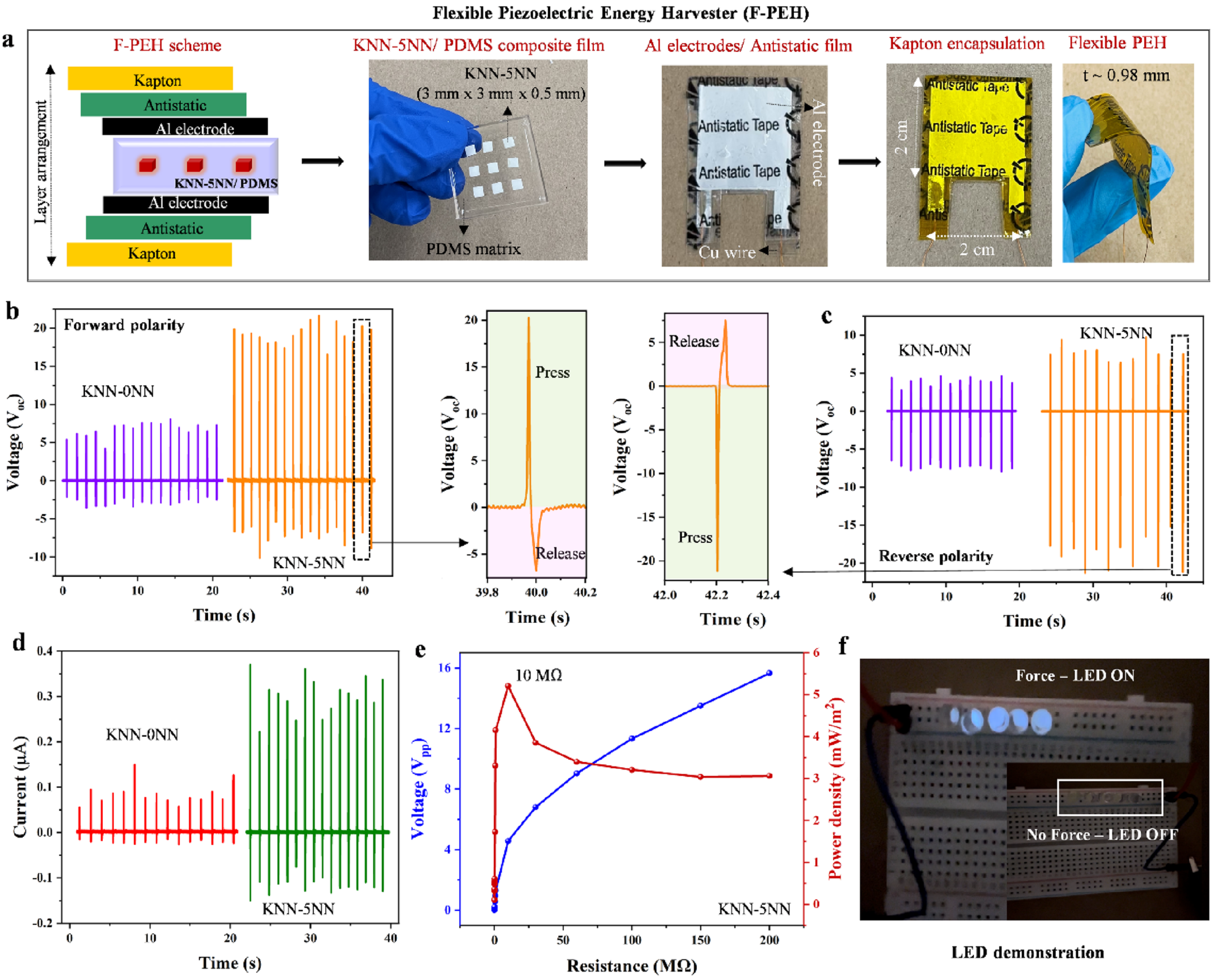

**Figure 5.** Development of the flexible piezoelectric energy harvester (F-PEH) using KNN-*x*NN ceramics. (a) Schematic of F-PEH design with the LbL arrangements and the digital photographs of the fabricated F-PEH. (b) Generated piezoelectric voltage response ($V_{oc}$) comparing the KNN-0NN- and KNN-5NN-based F-PEH and corresponding (c) switching polarity analysis. (d) Comparison of the piezoelectric current responses of KNN-0NN and KNN-5NN devices at 10 MΩ. (e) Power density of the KNN-5NN device as a function of load resistance ($R_L$). (f) Demonstration of the real-time application using KNN-5NN-based F-PEH to drive white LEDs.

Experimental Procedure, and the corresponding optical image of the process is shown in Figure 5a. The as-fabricated F-PEH has a thickness of ~0.98 mm, comprising of the layer-by-layer (LbL) arrangements of Kapton/antistatic tape/Al/KNN-*x*NN–PDMS/Al/antistatic tape/Kapton (Figure S12). An insulating polymer PDMS is preferred to provide flexibility to the F-PEH devices by acting as a supporting cross-linking stage to hold the KNN-*x*NN ceramic in place. Further, the dielectric property of PDMS helps to ensure that the electrical response of F-PEH is from the cumulative effects of KNN-*x*NN piezoelectric distributed inside the PDMS matrix. An antistatic layer is used to suppress the generation of electrostatic potentials due to the Al–Kapton interfacial effects. The Kapton/antistatic film/Al layering contributes zero electrical charges to the overall performance of F-PEH.[42,43]

The energy harvesting ability of F-PEH devices with an 18 wt % KNN-*x*NN composite film is assessed under biomechanical force through constant hand pressure. Before electrical measurements, the F-PEH devices are poled at a 6 kV DC electric field for 12 h at room temperature. Figure 5b compares the open-circuit voltage ($V_{oc}$) of random (18 wt % KNN-0NN) and textured (18 wt % KNN-5NN) sample-based F-PEH devices. Under constant force, the textured F-PEH device generates a higher peak-to-peak voltage ($V_{oc}$ ~ 25 V) than the random F-PEH ($V_{oc}$ ~ 8 V). The perpendicular force acting on the device modulates the orientation of the electrical dipoles, creating a potential difference across the top and bottom electrodes. Thus, when the device is pressed, the flow of the generated piezoelectric charge between the two electrodes results in a positive cycle. When released, the backflow of the electrical charges between the electrodes results in a negative cycle. The enlarged image of Figure 5b clearly shows the cyclic pattern of the measured signals. The results are validated by performing a switching polarity test as shown in Figure 5c. A complete phase shift in peaks is observed in terms of the positive and negative cycles during the force conditions (press and release). This reversible nature authenticates that the electrical output of F-PEH is from the intrinsic piezoelectric effect of KNN-*x*NN ceramics and is not influenced by any extrinsic parameters. Figure 5d shows the current responses of random ($I \sim 0.1\ \mu$A) and textured ($I \sim 0.4\ \mu$A) F-PEH devices at 10 MΩ determined by the load resistance ($R_L$) analysis. Figure 5e presents the load resistance-dependent voltage ($V_{pp}$) and power density ($P_D$) to identify the impedance matching for practical applications. The textured F-PEH device output voltage increases as the resistance increases from 50 Ω to 200 MΩ. The areal power density of F-PEH under constant force is represented as[43]

$$P_D = \frac{V^2}{R \times A} \tag{9}$$

where $V$ is the generated voltage, $R$ is the load resistance, and $A$ is the active device area (2 cm × 2 cm). From eq 9, the maximum power density of 5.5 mW/m$^2$ is obtained at 10 MΩ matching impedance. The F-PEH device constructed using the textured KNN-5NN ceramic exhibits a higher performance compared to the random counterpart depending on the piezo-potential generation, which can be related to[44]

$$V_{oc} = (d_{ij} \cdot \sigma \cdot Y \cdot t)/(\varepsilon_o \cdot K) \tag{10}$$

where $d_{ij}$ is the piezoelectric coefficient, $t$ is the thickness of the F-PEH device, $Y$ is Young's modulus, $\sigma$ is the perpendicular strain acting on the device, $K$ is the dielectric constant, and $\varepsilon_o$ is the relative permittivity of the ceramic. Correlating to the above equation, the enhanced performance of textured F-PEH can be attributed to the higher $d_{33}$ of ~590 pC/N exhibited by the KNN-5NN ceramic. Comparatively, KNN-0NN produces a lower $d_{33}$ of ~270 pC/N and, hence, the performance of F-PEH developed using the random ceramic shows a lower electrical voltage.

The performance of the textured device is evaluated based on the dimensionless figure of merit (DFOM).[45−47] For an energy harvester operating at an off-resonance frequency, the DFOM is given by

$$\mathrm{DFOM_{OFF}} = d_{31} \times g_{31} \tag{11}$$

The textured F-PEH with large $d_{31} \sim 215 \times 10^{-12}$ C/N and $g_{31} \sim 15.602 \times 10^{-3}$ Vm/N exhibits a high figure-of-merit value of $\sim 3354 \times 10^{-15}$ m$^3$/J. With relatively low tan $\delta \sim 0.0245$, the textured KNN-5NN-based F-PEH shows higher energy harvesting capability than the device developed using the random KNN-0NN ceramic having a high loss factor of ~0.0325. The generated electrical output from textured F-PEH is sufficient to drive commercially available low-power electronics. A real-time operation is demonstrated as shown in Figure 5f by powering white LEDs using the KNN-5NN ceramic-based F-PEH device. The ON/OFF behavior of the LEDs corresponds to the applied force conditions. Under no force, the LEDs are OFF as there is a zero net dipole moment in the F-PEH device. Upon applying force, the LEDs glow due to the stress-induced piezoelectric potentials, which are collected across the electrodes. The systematic analysis reveals that textured piezoceramics are potential candidates for energy harvesting applications. The KNN-5NN sample-based F-PEH shows the flexible characteristics of an energy harvester developed using textured (Table S2) and nontextured (Table S3) piezoceramics. This demonstration will provide new opportunities to design energy harvesters with higher power output by benefiting from the high-performing lead-free textured ceramics.

## ■ CONCLUSIONS

In summary, the textured KNN-$x$NN ceramics with high piezoelectric constants $k_{31} \sim 0.46$ and $d_{31} \sim 215 \times 10^{-12}$ C/N are synthesized through the template grain growth method with the addition of 5 wt % NaNbO$_3$ template. Compared to the random counterpart KNN-0NN, the textured KNN-5NN exhibits 94% orientation degree ($F$), improved room-temperature dielectric constant by 29.4% (1 kHz), $d_{33}$ by 54.2% (270 to 590 pC/N), remanent polarization by 41.5% (11.32 to 19.34 $\mu$C/cm$^2$ at 40 kV/cm), coercive field by 15.4% (11.61 to 13.72 kV/cm$^2$), and unipolar strain by 46% (0.15 to 0.28%). The flexible PEH fabricated using the 18 wt % textured KNN-5NN/PDMS composite film shows a high mechanical energy harvesting capability by generating $V_{oc} \sim 25$ V, $I \sim 0.4\ \mu$A, and $P_D \sim 5.5$ mW/m$^2$ than the 18 wt % random KNN-0NN-based F-PEH ($V_{oc} \sim 8$ V and $I \sim 0.1\ \mu$A). The produced energy is utilized to successfully drive the white LEDs. The constructed F-PEH has the better figure-of-merit $d_{31} \times g_{31}$ values by utilizing high-performance textured ceramics. The approach provides a new route to take advantage of textured ceramics to develop high-output power energy harvesters for wireless sensor nodes.

## ■ ASSOCIATED CONTENT

### Supporting Information

The Supporting Information is available free of charge at https://pubs.acs.org/doi/10.1021/acsami.2c15640.

> Figure S1: schematic illustration of KNN-$x$NN synthesis procedures; Figure S2: XRD and FESEM analysis of synthesized NaNbO$_3$ templates; Figure S3: relative density of the KNN-$x$NN ceramic as a function of sintering temperature and NN template ratio; Figure S4: FESEM image of 3 and 7 wt % KNN-$x$NN samples; Figure S5: EBSD micrographs; Figure S6: field- and temperature-dependent P−E loops of KNN-5NN; Figure S7: fatigue characteristic behavior of KNN-0NN; Figure S8: fatigue model illustrating the domain wall pinning and cracking mechanisms; Figure S9: phase transition of KNN-5NN ceramics at elevated temperatures; Figure S10: schematic illustration of the evolution of domains as a function of phase transition; Figure S11: temperature-dependent unipolar strain of random and textured ceramics; Figure S12: thickness profile of F-PEH devices using KNN-$x$NN ceramics; Table S1: summary of the performance values of KNN-0NN and KNN-5NN ceramics; Table S2: list of the models for PEH developed using textured ceramics; Table S3: comparison of the energy harvesting performances of KNN-5NN-based F-PEH with other published reports (PDF)

## ■ AUTHOR INFORMATION

### Corresponding Author

**Shashank Priya** − *Department of Materials Science and Engineering, The Pennsylvania State University, University Park, Pennsylvania 16802, United States*; Email: sup103@psu.edu

### Authors

**Yuvasree Purusothaman** − *Department of Materials Science and Engineering, The Pennsylvania State University,*

University Park, Pennsylvania 16802, United States; orcid.org/0000-0001-8834-4120

**Haoyang Leng** − Department of Materials Science and Engineering, The Pennsylvania State University, University Park, Pennsylvania 16802, United States; orcid.org/0000-0003-1402-7960

**Aman Nanda** − Department of Materials Science and Engineering, The Pennsylvania State University, University Park, Pennsylvania 16802, United States

**Ilan Levine** − Department of Physics and Astronomy, Indiana University, South Bend, Indiana 46615, United States

Complete contact information is available at: https://pubs.acs.org/10.1021/acsami.2c15640

## Notes

The authors declare no competing financial interest.

## ■ ACKNOWLEDGMENTS

The authors acknowledge the financial support from National Science Foundation through award number 1936432 (Y.P. and S.P.). H.L. acknowledges the support from Office of Naval Research through award number N000142012309. A.N. acknowledges the support from Office of Naval Research through award number N000141712088.

## ■ REFERENCES

(1) Kim, H.; Tadesse, Y.; Priya, S.*Piezoelectric Energy Harvesting*. Springer2009, 3−39.

(2) Hinchet, R.; Yoon, H. J.; Ryu, H.; Kim, M. K.; Choi, E. K.; Kim, D. S.; Kim, S. W. Transcutaneous Ultrasound Energy Harvesting Using Capacitive Triboelectric Technology. *Science* **2019**, *365*, 491−494.

(3) Nozariasbmarz, A.; Collins, H.; Dsouza, K.; Polash, M. H.; Hosseini, M.; Hyland, M.; Liu, J.; Malhotra, A.; Ortiz, F. M.; Mohaddes, F.; Ramesh, V. P.; Sargolzaeiaval, Y.; Snouwaert, N.; Özturk, M. C.; Vashaee, D. Review of Wearable Thermoelectric Energy Harvesting: From Body Temperature to Electronic Systems. *Appl. Energy* **2020**, *258*, No. 114069.

(4) Pandya, S.; Velarde, G.; Zhang, L.; Wilbur, J. D.; Smith, A.; Hanrahan, B.; Dames, C.; Martin, L. W. New Approach to Waste-Heat Energy Harvesting: Pyroelectric Energy Conversion. *NPG Asia Mater.* **2019**, *11*, 26.

(5) Hao, D.; Qi, L.; Tairab, A. M.; Ahmed, A.; Azam, A.; Luo, D.; Pan, Y.; Zhang, Z.; Yan, J. Solar Energy Harvesting Technologies for PV Self-Powered Applications: A Comprehensive Review. *Renewable Energy* **2022**, *188*, 678−697.

(6) Mahapatra, S. D.; Mohapatra, P. C.; Aria, A. I.; Christie, G.; Mishra, Y. K.; Hofmann, S.; Thakur, V. K. Piezoelectric Materials for Energy Harvesting and Sensing Applications: Roadmap for Future Smart Materials. *Adv. Sci.* **2021**, *8*, 2100864.

(7) Wang, H. S.; Hong, S. K.; Han, J. H.; Jung, Y. H.; Jeong, H. K.; Im, T. H.; Jeong, C. K.; Lee, B. Y.; Kim, G.; Yoo, C. D.; Lee, K. J. Biomimetic and Flexible Piezoelectric Mobile Acoustic Sensors with Multiresonant Ultrathin Structures for Machine Learning Biometrics. *Sci. Adv.* **2021**, *7*, 1−9.

(8) Priya, S.; Song, H.-C.; Zhou, Y.; Varghese, R.; Chopra, A.; Kim, S.-G.; Kanno, I.; Wu, L.; Ha, D. S.; Ryu, J.; Polcawich, R. G. A Review on Piezoelectric Energy Harvesting: Materials, Methods, and Circuits. *Energy Harvest. Syst.* **2019**, *4*, 3−39.

(9) Safari, A.; Akdogan, E. K., Eds *Piezoelectric and Acoustic Materials for Transducer Applications*. Springer, 2008,496, DOI: 10.1007/978-0-387-76540-2.

(10) Liu, H.; Yan, Y.; Leng, H.; Heitmann, A.; Blottman, J. B.; Priya, S. High Performance High Power Textured Piezoceramics. *Appl. Phys. Lett.* **2020**, *116*, 1−6.

(11) Bell, A. J.; Deubzer, O. Lead-Free Piezoelectrics - The Environmental and Regulatory Issues. *MRS Bull.* **2018**, *43*, 581−587.

(12) Priya, S.; Nahm, S.*Lead-Free Piezoelectrics*. Springer2012, *1*, 528.

(13) Panda, P. K. Review: Environmental Friendly Lead-Free Piezoelectric Materials. *J. Mater. Sci.* **2009**, *44*, 5049−5062.

(14) Wu, J.; Xiao, D.; Zhu, J. Potassium-Sodium Niobate Lead-Free Piezoelectric Materials: Past, Present, and Future of Phase Boundaries. *Chem. Rev.* **2015**, *115*, 2559−2595.

(15) Shirane, G.; Newnham, R.; Pepinsky, R. Dielectric Properties and Phase Transitions of $NaNbO_3$ and $(Na,K)NbO_3$. *Phys. Rev.* **1954**, *96*, 581−588.

(16) Lv, X.; Zhu, J.; Xiao, D.; Zhang, X. X.; Wu, J. Emerging New Phase Boundary in Potassium Sodium-Niobate Based Ceramics. *Chem. Soc. Rev.* **2020**, *49*, 671−707.

(17) Li, J. F.; Wang, K.; Zhu, F. Y.; Cheng, L. Q.; Yao, F. Z. $(K,Na)NbO_3$-Based Lead-Free Piezoceramics: Fundamental Aspects, Processing Technologies, and Remaining Challenges. *J. Am. Ceram. Soc.* **2013**, *96*, 3677−3696.

(18) Hollenstein, E.; Davis, M.; Damjanovic, D.; Setter, N. Piezoelectric Properties of Li- and Ta-Modified $(K_{0.5}Na_{0.5})NbO_3$ Ceramics. *Appl. Phys. Lett.* **2005**, *87*, 182905.

(19) Skidmore, T. A.; Comyn, T. P.; Bell, A. J.; Zhu, F.; Milne, S. J. Phase Diagram and Structure-Property Relationships in the Lead-Free Piezoelectric System: $Na_{0.5}K_{0.5}NbO_3$-$LiTaO_3$. *IEEE Trans. Plasma Sci.* **2008**, *36*, 1819−1825.

(20) Kroutvar, M.; Ducommun, Y.; Heiss, D.; Bichler, M.; Schuh, D.; Abstreiter, G.; Finley, J. J. Optically Programmable Electron Spin Memory Using Semiconductor Quantum Dots. *Nature* **2004**, *432*, 81−84.

(21) Li, P.; Zhai, J.; Shen, B.; Zhang, S.; Li, X.; Zhu, F.; Zhang, X. Ultrahigh Piezoelectric Properties in Textured $(K,Na)NbO_3$-Based Lead-Free Ceramics. *Adv. Mater.* **2018**, *30*, 1705171.

(22) Chae, S. J.; Na, J.; Kim, D. S.; Kim, S.-W.; Go, S.-H.; Kim, H.; Kim, E.-J.; Eum, J.-M.; Nahm, S. Application of [001]-Textured (K, Na)(Nb, Sb)$O_3$-$CaZrO_3$ Thick Films to Piezoelectric Energy Harvesters. *Ceram. Int.* **2022**, *48*, 18401−18414.

(23) Chang, Y.; Yang, Z.; Chao, X.; Liu, Z.; Wang, Z. Synthesis and Morphology of Anisotropic $NaNbO_3$ Seed Crystals. *Mater. Chem. Phys.* **2008**, *111*, 195−200.

(24) Moriana, A. D.; Zhang, S. Lead-Free Textured Piezoceramics Using Tape Casting: A Review. *J. Mater.* **2018**, *4*, 277−303.

(25) Yang, S.; Li, J.; Liu, Y.; Wang, M.; Qiao, L.; Gao, X.; Chang, Y.; Du, H.; Xu, Z.; Zhang, S.; Li, F. Textured Ferroelectric Ceramics with High Electromechanical Coupling Factors over a Broad Temperature Range. *Nat. Commun.* **2021**, *12*, 1−10.

(26) Skidmore, T. A.; Milne, S. J. Phase Development during Mixed-Oxide Processing of a $[Na_{0.5}K_{0.5}NbO_3]_{1-x}$-$[LiTaO_3]_x$ Powder. *J. Mater. Res.* **2007**, *22*, 2265−2272.

(27) Zhou, J.; Xiang, G.; Shen, J.; Zhang, H.; Xu, Z.; Li, H.; Ma, P.; Chen, W. Composition-Insensitive Enhanced Piezoelectric Properties in $SrZrO_3$ Modified ( $K,Na)NbO_3$ -Based Lead-Free Ceramics. *J. Electroceram.* **2020**, *44*, 95−103.

(28) Jones, J. L.; Iverson, B. J.; Bowman, K. J. Texture and Anisotropy of Polycrystalline Piezoelectrics. *J. Am. Ceram. Soc.* **2007**, *90*, 2297−2314.

(29) Jin, L.; Li, F.; Zhang, S. Decoding the Fingerprint of Ferroelectric Loops: Comprehension of the Material Properties and Structures. *J. Am. Ceram. Soc.* **2014**, *97*, 1−27.

(30) Zheng, T.; Wu, H.; Yuan, Y.; Lv, X.; Li, Q.; Men, T.; Zhao, C.; Xiao, D.; Wu, J.; Wang, K.; Li, J. F.; Gu, Y.; Zhu, J.; Pennycook, S. J. The Structural Origin of Enhanced Piezoelectric Performance and Stability in Lead Free Ceramics. *Energy Environ. Sci.* **2017**, *10*, 528−537.

(31) Genenko, Y. A.; Glaum, J.; Hoffmann, M. J.; Albe, K. Mechanisms of Aging and Fatigue in Ferroelectrics. *Mater. Sci. Eng. B* **2015**, *192*, 52−82.

(32) American, A.; Standard, N. An American National Standard: IEEE Standard on Piezoelectricity. *IEEE Trans. Sonics Ultrason.* **1984**, *31*, 8−10.

(33) Ahn, C. W.; Park, C. S.; Viehland, D.; Nahm, S.; Kang, D. H.; Bae, K. S.; Priya, S. Correlation between Phase Transitions and Piezoelectric Properties in Lead-Free (K,Na,Li)$\mathrm{NbO_3}$-$\mathrm{BaTiO_3}$ Ceramics. *Jpn. J. Appl. Phys.* **2008**, *47*, 8880−8883.

(34) Li, P.; Chen, X.; Wang, F.; Shen, B.; Zhai, J.; Zhang, S.; Zhou, Z. Microscopic Insight into Electric Fatigue Resistance and Thermally Stable Piezoelectric Properties of (K,Na)$\mathrm{NbO_3}$-Based Ceramics. *ACS Appl. Mater. Interfaces* **2018**, *10*, 28772−28779.

(35) Shi, X.; Kumar, N.; Hoffman, M. Electrical Fatigue Behavior of NBT-BT-xKNN Ferroelectrics: Effect of Phase Transformations and Oxygen Vacancies. *J. Mater. Chem. C* **2020**, *8*, 3887−3896.

(36) Ma, H.-S.; Lee, M.-K.; Kim, B.-H.; Park, K.-H.; Park, J.-J.; Lee, S.-H.; Jeong, Y.-G.; Park, K.-I.; Jeong, C. K.; Lee, G.-J. Role of Oxygen Vacancy Defects in Piezoelectric Thermal Stability Characteristics of Mn-Doped (K,Na,Li)$\mathrm{NbO_3}$ Piezoceramics. *Ceram. Int.* **2021**, *47*, 27803−27815.

(37) Du, H.; Zhou, W.; Luo, F.; Zhu, D.; Qu, S.; Li, Y.; Pei, Z. Polymorphic Phase Transition Dependence of Piezoelectric Properties in $\mathrm{(K_{0.5}Na_{0.5})NbO_3}$-$\mathrm{(Bi_{0.5}K_{0.5})TiO_3}$ Lead-Free Ceramics. *J. Phys. D. Appl. Phys.* **2008**, *41*, No. 115413.

(38) Hollenstein, E.; Damjanovic, D.; Setter, N. Temperature Stability of the Piezoelectric Properties of Li-Modified KNN Ceramics. *J. Eur. Ceram. Soc.* **2007**, *27*, 4093−4097.

(39) Yang, W.; Wang, Y.; Li, P.; Li, P.; Wu, S.; Wang, F.; Shen, B.; Zhai, J. Improving Electromechanical Properties in KNANS-BNZ Ceramics by the Synergy between Phase Structure Modification and Grain Orientation. *J. Mater. Chem. C* **2020**, *8*, 6149−6158.

(40) Yang, W.; Li, P.; Wu, S.; Li, F.; Shen, B.; Zhai, J. Coexistence of Excellent Piezoelectric Performance and Thermal Stability in KNN-Based Lead-Free Piezoelectric Ceramics. *Ceram. Int.* **2020**, *46*, 1390−1395.

(41) Yang, W.; Li, P.; Wu, S.; Li, F.; Shen, B.; Zhai, J. A Study on the Relationship Between Grain Size and Electrical Properties in (K,Na)$\mathrm{NbO_3}$-Based Lead-Free Piezoelectric Ceramics. *Adv. Electron. Mater.* **2019**, *5*, 1900570.

(42) Zou, H.; Zhang, Y.; Guo, L.; Wang, P.; He, X.; Dai, G.; Zheng, H.; Chen, C.; Wang, A. C.; Xu, C.; Wang, Z. L. Quantifying the Triboelectric Series. *Nat. Commun.* **2019**, *10*, 1−9.

(43) Purusothaman, Y.; Alluri, N. R.; Chandrasekhar, A.; Kim, S. J. Photoactive Piezoelectric Energy Harvester Driven by Antimony Sulfoiodide (SbSI): A $\mathrm{A^{V}B^{VI}C^{VII}}$ Class Ferroelectric-Semiconductor Compound. *Nano Energy* **2018**, *50*, 256−265.

(44) Li, L.; Xu, J.; Liu, J.; Gao, F. Recent Progress on Piezoelectric Energy Harvesting: Structures and Materials. *Adv. Compos. Hybrid Mater.* **2018**, *1*, 478−505.

(45) Xu, R.; Kim, S. G. Figures of Merits of Piezoelectric Materials in Energy. *PowerMEMS* **2012**, 464−467.

(46) Liu, Y.; Khanbareh, H.; Halim, M. A.; Feeney, A.; Zhang, X.; Heidari, H.; Ghannam, R. Piezoelectric Energy Harvesting for Self-powered Wearable Upper Limb Applications. *Nano Sel.* **2021**, *2*, 1459−1479.

(47) Li, T.; Lee, P. S. Piezoelectric Energy Harvesting Technology: From Materials, Structures, to Applications. *Small Struct.* **2022**, *3*, 2100128.

Recommended by ACS

**High Piezoelectricity in Eco-Friendly $\mathrm{NaNbO_3}$-Based Ferroelectric Relaxor Ceramics via Phase and Domain Engineering**
Yingbo Cao, Jiwei Zhai, *et al.*
JANUARY 19, 2023
ACS APPLIED MATERIALS & INTERFACES
READ

**Design of a KNN-BZT Ceramic with High Energy Storage Properties and Transmittance under Low Electric Fields**
Zhonghua Dai, Shintaro Yasui, *et al.*
FEBRUARY 14, 2023
ACS OMEGA
READ

**Utilization of Nonstoichiometric $\mathrm{Nb^{5+}}$ to Optimize Comprehensive Electrical Properties of KNN-Based Ceramics**
Hongjiang Li, Jianguo Zhu, *et al.*
NOVEMBER 11, 2022
INORGANIC CHEMISTRY
READ

**Molten-Salt Processed Potassium Sodium Niobate Single-Crystal Microcuboids with Dislocation-Induced Nanodomain Structures and Relaxor Ferroelectric Behavior**
Seonhwa Park, Yuho Min, *et al.*
SEPTEMBER 08, 2022
ACS NANO
READ

Get More Suggestions >